공학석사 학위논문

Elastic reverse time migration strategy for multicomponent ocean-bottom cable data

다성분 해저면 탄성파 탐사 자료 역시간 구조보정 전략

2021년 2월

서울대학교 대학원
에너지시스템공학부
이진형

Elastic reverse time migration strategy for multicomponent ocean−bottom cable data

다성분 해저면 탄성파 탐사 자료 역시간 구조보정 전략

지도교수 민 동 주

이 논문을 공학석사학위논문으로 제출함
2021년 1월

서울대학교 대학원
공과대학 에너지시스템공학부

이 진 형

이진형의 공학석사학위논문을 인준함
2021년 1월

위 원 장 민 기 복 (인)

부위원장 민 동 주 (인)

위 원 정 은 혜 (인)

Abstract

Elastic reverse time migration strategy for multicomponent ocean-bottom cable data

Jinhyung Lee
Department of Energy Systems Engineering
The Graduate School
Seoul National University

Reverse time migration (RTM), which provides accurate subsurface images even for complicated structures, has been intensively studied. Most of studies have devoted to developing RTM algorithms for acoustic or elastic data. As the multicomponent ocean-bottom cable (OBC) survey using both hydrophones and geophones has become common in oil and gas explorations, the strategy for RTM of the multicomponent OBC data is needed. Because the acquisition geometry of OBC is closer to subsurface targets than that of the surface survey, OBC data generally have high signal-to-noise ratio, and the enhanced coverage. In case of using both hydrophones and geophones, additional information can be used.

In this study, I propose an elastic RTM strategy for multicomponent OBC data. The staggered-grid method is chosen due to its advantage in describing the fluid-solid interface. The strategy is first applied to synthetic data to investigate the effects of the imaging conditions and data components. Results for the synthetic data show that the PP image obtained by using the vertical-component data accurately describes P-wave velocity structures, and the PS image obtained with the horizontal-component data is good for the reconstruction of S-wave velocity structures.

The proposed strategy is then applied to the Volve oilfield data acquired in the North Sea. The RTM images successfully describe the known geological structures. The real data examples show that the P- and S-wave velocity structures in the PP and PS images obtained by RTM are in good agreement with the well log data.

Keyword: reverse time migration (RTM), elastic, ocean-bottom cable (OBC), staggered-grid, PS decomposition

Student Number: 2019-28629

Contents

Figures

Chapter 1. Introduction

1.1. Background of the study

Seismic method has been mainly used for gas and oil exploration. The seismic wave generated from sources is refracted or reflected depending on properties of subsurface media. Accordingly, the properties such as the P-wave and S-wave velocities can be determined from signals recorded at receivers. Wave propagation can be numerically simulated based on the wave equations, which is called forward modeling. Many studies have been devoted to lowering the computational cost and to enhancing the accuracy of modeling results. The finite-differential method (FDM) using nine points can decrease the number of grid points per wavelength (Jo et al., 1996). Min et al. (2004) proposed the cell-based FDM to properly describe the free-surface boundary condition in elastic models. Virieux (1984) and Graves (1996) used the staggered-grid FDM in the time domain to describe wave propagation in acoustic-elastic coupled media.

Inversion, tomography and migration are the methods used to estimate physical properties or image structures of subsurface media. Among them, migration is the data processing technique to image subsurface structures by returning refracted or reflected signals into their original points. Migration is classified as prestack/poststack and time/depth migration. Kirchhoff migration assumes that every point can be regarded as a diffraction point, and summing recorded data along the diffraction curve at every point plays a role in gathering energy to the diffraction point (Schneider, 1978). In order to determine the location of diffractions points, traveltimes between shots and diffraction points should be calculated. Although Kirchhoff migration requires the low computational cost, it can be inaccurate for complicated models.

Accordingly, reverse time migration (RTM) was proposed (Baysal et al. 1983; McMechan, 1983; Whitmore, 1983). RTM requires the high computational cost because it is based on the wave equations. Nevertheless, it has been intensively studied because it can provide accurate images even for complicated models. Lailly (1983) and Tarantola (1984) showed that RTM image and the first gradient of full waveform inversion (FWI) are the same. Shin et al. (2001) used the Hessian matrix in order to enhance the image of the deep part. Guitton et al. (2007) applied various filters to RTM images to remove artifacts arising where the velocities abruptly vary. The wavefield in elastic media can be decomposed into the potentials using the Helmholtz decomposition in the time (Yan and Sava, 2008) and frequency domains (Chung, 2011).

1.2. Purpose of Research

Recently, the multicomponent seismic survey using both streamer and ocean-bottom cable (OBC) is commonly performed (Park et al., 2018; Shinn et al., 2018). Multicomponent OBC data have advantages of the high signal-to-noise ratio (SNR) and enhanced coverage, because data are acquired near the sea bottom. Also more information is available, because the S-waves are recorded as well as the P-waves. Accordingly, strategies for using multicomponent data has been studied. Hwang et al. (2020) proposed acoustic FWI strategy for multicomponent ocean-bottom cable (OBC) data.

This study aims to propose the elastic RTM strategy for multicomponent data to successfully image the P- and S-wave structures. The strategy is developed considering the modeling grid set, imaging condition, and data components. The proposed strategy is demonstrated for synthetic and real data.

1.3. Outline

This thesis is organized as follows: In Chapter 2, frequency-domain staggered-grid FDM modeling and boundary conditions will be reviewed. Then, advantages of the staggered-grid set for acoustic-elastic coupled models will be discussed. In Chapter 3, the concept and imaging conditions of RTM will be introduced. The characteristics of the images obtained by the imaging conditions will be described. After that, the strategies to efficiently use multicomponent data will be proposed, and all the strategies will be demonstrated for synthetic data. In Chapter 4, the feasibility of the proposed strategy will be applied to real data acquired in the Volve oilfield of the North Sea. In Chapter 5, Conclusion will be provided.

Chapter 2. Elastic wave modeling in the staggered-grid set

2.1. Staggered-grid FDM in the frequency domain

The equation of motion in a two-dimensional (2D) elastic medium is expressed by the Newton's second law as follows:

$$\rho \frac{d^2 u_x}{dt^2} = \frac{\partial \tau_{xx}}{\partial x} + \frac{\partial \tau_{xz}}{\partial z}, \tag{2-1}$$

$$\rho \frac{d^2 u_z}{dt^2} = \frac{\partial \tau_{zx}}{\partial x} + \frac{\partial \tau_{zz}}{\partial z}, \tag{2-2}$$

where u_i denotes the i-direction particle displacement, τ_{ij} denotes the stress acting in the j-direction on the plane with a normal in the i-direction, and ρ denotes the density. The stress-strain relationship in an isotropic elastic medium can be defined by the Hooke's law as follows:

$$\tau_{xx} = (\lambda + 2\mu)\frac{\partial u_x}{\partial x} + \lambda \frac{\partial u_z}{\partial z}, \tag{2-3}$$

$$\tau_{xz} = \mu \left(\frac{\partial u_z}{\partial x} + \frac{\partial u_x}{\partial z}\right), \tag{2-4}$$

$$\tau_{zz} = \lambda \frac{\partial u_x}{\partial x} + (\lambda + 2\mu) \frac{\partial u_z}{\partial z}, \tag{2-5}$$

where λ and μ are the Lame's constants. The 2D wave equation in the time domain can be derived by substituting the Hooke's law for the equation of motion as follows:

$$\rho \frac{d^2 u_x}{dt^2} = \frac{\partial}{\partial x}\left((\lambda + 2\mu) \frac{\partial u_x}{\partial x} + \lambda \frac{\partial u_z}{\partial z} \right) + \frac{\partial}{\partial z}\left(\mu \left(\frac{\partial u_z}{\partial x} + \frac{\partial u_x}{\partial z} \right) \right), \tag{2-6}$$

$$\rho \frac{d^2 u_z}{dt^2} = \frac{\partial}{\partial x}\left(\mu \left(\frac{\partial u_z}{\partial x} + \frac{\partial u_x}{\partial z} \right) \right) + \frac{\partial}{\partial z}\left(\lambda \frac{\partial u_x}{\partial x} + (\lambda + 2\mu) \frac{\partial u_z}{\partial z} \right). \tag{2-7}$$

Modeling can be performed in the time/frequency domain and space/wavenumber domain. The 2D wave equation in the frequency domain can be derived by the Fourier transform of the wave equation in the time domain as follows:

$$\rho \omega^2 \tilde{u}_x = \frac{\partial}{\partial x}\left((\lambda + 2\mu) \frac{\partial \tilde{u}_x}{\partial x} + \lambda \frac{\partial \tilde{u}_z}{\partial z} \right) + \frac{\partial}{\partial z}\left(\mu \left(\frac{\partial \tilde{u}_z}{\partial x} + \frac{\partial \tilde{u}_x}{\partial z} \right) \right), \tag{2-8}$$

$$\rho \omega^2 \tilde{u}_z = \frac{\partial}{\partial x}\left(\mu \left(\frac{\partial \tilde{u}_z}{\partial x} + \frac{\partial \tilde{u}_x}{\partial z} \right) \right) + \frac{\partial}{\partial z}\left(\lambda \frac{\partial \tilde{u}_x}{\partial x} + (\lambda + 2\mu) \frac{\partial \tilde{u}_z}{\partial z} \right). \tag{2-9}$$

While time-domain modeling is sequentially performed, frequency-domain modeling is independently carried out across frequencies. Therefore, the parallel computation is easier to carry out in the frequency domain than in the time domain. Furthermore, once the modeling operator is composed, it can be repeatedly used for different sources, because the modeling operator is constructed independently of source locations. For these reasons, frequency-domain modeling has been commonly used for full waveform inversion or reverse time migration.

The wave equation in the frequency domain can be expressed as FDM in staggered-grid shown in Figure 2-1 as follows:

$$
\begin{aligned}
&\frac{\rho(i,j)+\rho(i+1,j)}{2}\omega^2\tilde{u}_x\left(\mathrm{i}+\frac{1}{2},\mathrm{j}\right) \\
&\quad=\frac{1}{\Delta x}\left[\left\{C_{11}(i+1,j)\frac{\tilde{u}_x\left(\mathrm{i}+\frac{3}{2},\mathrm{j}\right)-\tilde{u}_x\left(\mathrm{i}+\frac{1}{2},\mathrm{j}\right)}{\Delta x}+C_{13}(i+1,j)\frac{\tilde{u}_z\left(\mathrm{i}+1,\mathrm{j}+\frac{1}{2}\right)-\tilde{u}_z\left(\mathrm{i}+1,\mathrm{j}-\frac{1}{2}\right)}{\Delta z}\right\}\right. \\
&\quad\left.-\left\{C_{11}(i,j)\frac{\tilde{u}_x\left(\mathrm{i}+\frac{1}{2},\mathrm{j}\right)-\tilde{u}_x\left(\mathrm{i}-\frac{1}{2},\mathrm{j}\right)}{\Delta x}+C_{13}(i,j)\frac{\tilde{u}_z\left(\mathrm{i},\mathrm{j}+\frac{1}{2}\right)-\tilde{u}_z\left(\mathrm{i},\mathrm{j}-\frac{1}{2}\right)}{\Delta z}\right\}\right] \\
&\quad+\frac{1}{\Delta z}\left[\frac{C_{55}(i,j)+C_{55}(i+1,j)+C_{55}(i,j+1)+C_{55}(i+1,j+1)}{4}\right. \\
&\quad\times\left\{\frac{\tilde{u}_z\left(\mathrm{i}+1,\mathrm{j}+\frac{1}{2}\right)-\tilde{u}_z\left(\mathrm{i},\mathrm{j}+\frac{1}{2}\right)}{\Delta x}+\frac{\tilde{u}_x\left(\mathrm{i}+\frac{1}{2},\mathrm{j}+1\right)-\tilde{u}_x\left(\mathrm{i}+\frac{1}{2},\mathrm{j}\right)}{\Delta z}\right\} \\
&\quad-\frac{C_{55}(i,j-1)+C_{55}(i+1,j-1)+C_{55}(i,j)+C_{55}(i+1,j)}{4} \\
&\quad\left.\times\left\{\frac{\tilde{u}_z\left(\mathrm{i}+1,\mathrm{j}-\frac{1}{2}\right)-\tilde{u}_z\left(\mathrm{i},\mathrm{j}-\frac{1}{2}\right)}{\Delta x}+\frac{\tilde{u}_x\left(\mathrm{i}+\frac{1}{2},\mathrm{j}\right)-\tilde{u}_x\left(\mathrm{i}+\frac{1}{2},\mathrm{j}-1\right)}{\Delta z}\right\}\right]
\end{aligned}
\tag{2-10}
$$

$$
\begin{aligned}
&\frac{\rho(i,j)+\rho(i,j+1)}{2}\omega^2\tilde{u}_z\left(\mathrm{i},\mathrm{j}+\frac{1}{2}\right)\\
&\quad=\frac{1}{\Delta z}\left[\left\{C_{33}(i,j+1)\frac{\tilde{u}_z\left(\mathrm{i},\mathrm{j}+\frac{3}{2}\right)-\tilde{u}_z\left(\mathrm{i},\mathrm{j}+\frac{1}{2}\right)}{\Delta z}+C_{13}(i,j+1)\frac{\tilde{u}_x\left(\mathrm{i}+\frac{1}{2},\mathrm{j}+1\right)-\tilde{u}_x\left(\mathrm{i}-\frac{1}{2},\mathrm{j}+1\right)}{\Delta x}\right\}\right.\\
&\quad\left.-\left\{C_{33}(i,j)\frac{\tilde{u}_z\left(\mathrm{i},\mathrm{j}+\frac{1}{2}\right)-\tilde{u}_z\left(\mathrm{i},\mathrm{j}-\frac{1}{2}\right)}{\Delta z}+C_{13}(i,j)\frac{\tilde{u}_x\left(\mathrm{i}+\frac{1}{2},\mathrm{j}\right)-\tilde{u}_x\left(\mathrm{i}-\frac{1}{2},\mathrm{j}\right)}{\Delta x}\right\}\right]\\
&\quad+\frac{1}{\Delta x}\left[\frac{C_{55}(i,j)+C_{55}(i+1,j)+C_{55}(i,j+1)+C_{55}(i+1,j+1)}{4}\right.\\
&\quad\times\left\{\frac{\tilde{u}_x\left(\mathrm{i}+\frac{1}{2},\mathrm{j}+1\right)-\tilde{u}_x\left(\mathrm{i}+\frac{1}{2},\mathrm{j}\right)}{\Delta z}+\frac{\tilde{u}_z\left(\mathrm{i}+1,\mathrm{j}+\frac{1}{2}\right)-\tilde{u}_z\left(\mathrm{i},\mathrm{j}+\frac{1}{2}\right)}{\Delta x}\right\}\\
&\quad-\frac{C_{55}(i-1,j)+C_{55}(i,j)+C_{55}(i-1,j+1)+C_{55}(i,j+1)}{4}\\
&\quad\left.\times\left\{\frac{\tilde{u}_x\left(\mathrm{i}-\frac{1}{2},\mathrm{j}+1\right)-\tilde{u}_x\left(\mathrm{i}-\frac{1}{2},\mathrm{j}\right)}{\Delta z}+\frac{\tilde{u}_z\left(\mathrm{i},\mathrm{j}+\frac{1}{2}\right)-\tilde{u}_z\left(\mathrm{i}-1,\mathrm{j}+\frac{1}{2}\right)}{\Delta x}\right\}\right]
\end{aligned}
\tag{2-11}
$$

$(C_{11}=C_{33}=\lambda+2\mu, C_{13}=\lambda, C_{55}=\mu)$

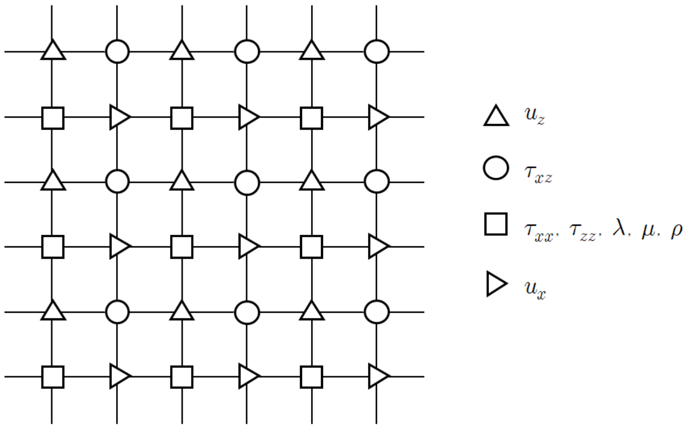

Figure 2-1. A staggered-grid for 2D elastic modeling.

2.2. Boundary conditions

While the real earth media is infinite, the modeling region is finite. To attenuate the unwanted reflections arising from the finite-sized modeling region, a boundary condition should be applied. A number of boundary conditions were developed. Among various boundary conditions, the perfectly matched layer (PML) has been widely used, which attenuates unwanted reflection waves by adding the attenuation term to the spatial term in the absorbing layer (Berenger, 1994; Collino and Tsogka, 1998). A monotonously increasing continuous function is used for the right boundary, and a monotonously decreasing continuous function is applied for the left boundary, which are expressed as follows:

$$A_0 e^{i(kx-\omega t)} \rightarrow A_0 e^{i\{k[x+if(x)]-\omega t\}} = A_0 e^{i(kx-\omega t)} e^{-kf(x)}, \tag{2-11}$$

$$A_0 e^{i(-kx-\omega t)} \rightarrow A_0 e^{i\{-k[x+if(x)]-\omega t\}} = A_0 e^{i(-kx-\omega t)} e^{kf(x)}, \tag{2-12}$$

where A_0 denotes the amplitude and k denotes the wavenumber. The spatial differential operator is modified as follows:

$$\begin{aligned} \frac{\partial}{\partial x} \rightarrow \frac{\partial}{\partial \tilde{x}} &= \frac{\partial}{\partial [x+if(x)]} = \frac{\partial}{\partial x} \frac{1}{1+i\dfrac{\partial f(x)}{\partial x}} \\ &= \frac{\partial}{\partial x} \frac{\omega i}{\omega i - \omega \dfrac{\partial f(x)}{\partial x}} = \frac{\partial}{\partial x} \frac{\omega i}{\omega i - d(x)}. \end{aligned} \tag{2-13}$$

The quadratic function is commonly used as a damping function $d(x)$ as follows:

$$d(x) = d_0 \left(\frac{x}{\delta}\right)^2, \tag{2-14}$$

$$d_0 = \ln(1000)\frac{3v}{2\delta}, \tag{2-15}$$

where δ denotes the thickness of the PML zone. Figure 2-2 shows seismograms obtained with and without the PML boundary condition. Waves reflected from the right, left and bottom boundaries were effectively removed by the PML boundary condition.

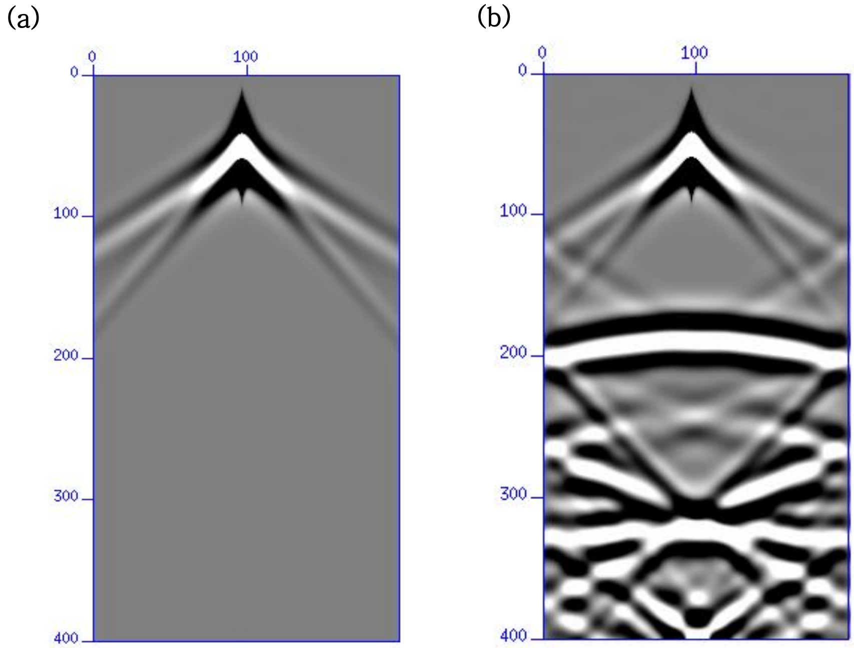

Figure 2-2. Shot gathers obtained by 2D elastic modeling (a) with and (b) without the PML boundary condition.

2.3. Coupled media modeling

In the early stage, targets of oil and gas exploration are in shallow depths and their geological structures are not complicated. As oil and gas have been continually developed, remains are located in deep and complicated structures. Accordingly, deep-sea surveys are commonly carried out in recent years. To correctly simulate marine environments with fluid-solid combined, a modeling engine describing the fluid-solid boundary condition accurately is required. The staggered-grid FDM has advantages in the aspects of stability and feasibility, because it satisfies the fluid-solid boundary condition without applying additional conditions (Shin et al., 1997).

The advantages of the staggered-grid modeling scheme are demonstrated for a two-layer model consisting of fluid and solid. The P- and S-wave velocities of the upper layer are assumed to be 1.5 km/s and 0 km/s, respectively. The P- and S-wave velocities of the lower layer are 3 km/s and 1.6 km/s, respectively. The densities of the upper and lower layer are 1 g/ml and 2.5 g/ml. A source is applied in the middle of the surface. Figure 2-3 shows a snapshot obtained with the staggered-grid FDM for the two-layer model. In the upper layer, only the P-wave propagates. When it encounters the fluid-solid boundary, the reflected P-wave, transmitted P-wave and transmitted S-wave are generated. The phase shift between incident P-wave and reflected P-wave is 180°.

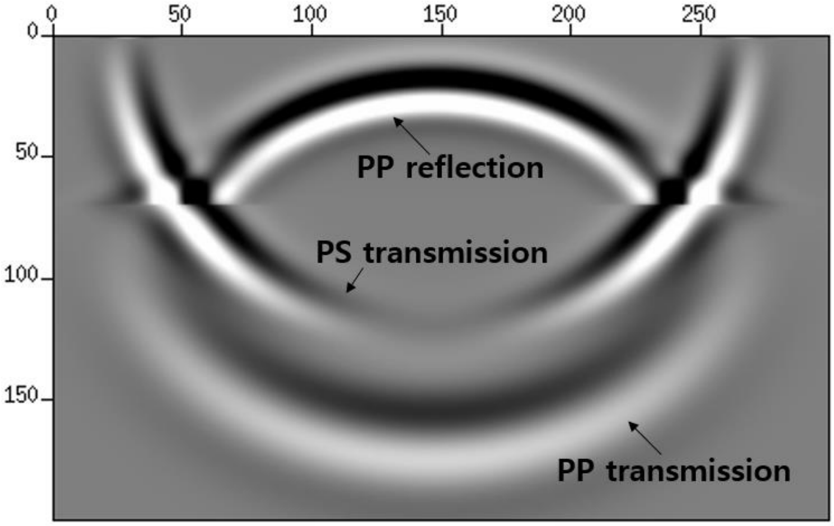

Figure 2-3. Snapshot for the fluid-solid coupled model.

Chapter 3. RTM strategy for multicomponent data

3.1. The concept of RTM

RTM images are calculated by cross-correlation of source wavefield and receiver wavefield. It is based on the assumption that source wavefields consist of downgoing waves and receiver wavefields consist of upcoming waves. In order to satisfy this condition, it is desirable to use one-way wave equation. However, one-way wave equations have disadvantages that the propagation angles are limited, and it is difficult to describe complicated structures and abrupt, lateral velocity changes. For this reason, two-way wave equations have been commonly used.

RTM images are calculated as follows:

$$\mathrm{I}(\mathrm{x},\mathrm{z}) = \sum_{s}\sum_{t} S_s(t,x,z)R_s(t,x,z), \tag{3-1}$$

where S denotes the source wavefield and R indicates the receiver wavefield. Source wavefields are obtained by propagating a source wavefield in a velocity model, whereas receiver wavefields are obtained by backpropagating observed data as a source in the velocity model. In the frequency domain, RTM images are calculated as follows:

$$\mathrm{I}(\mathrm{x}, \mathrm{z}) = \sum_{s} \sum_{\omega} \tilde{S}_s(\omega, x, z) \tilde{R}_s(\omega, x, z). \tag{3-2}$$

3.2. Strategy for imaging conditions

It is difficult to obtain clear RTM images in elastic media because elastic media generate the P-, S-, surface, and mode-converted waves. In order to solve this problem, RTM can be performed after the horizontal and vertical vectors are separated into the potentials of the P- and S-waves using the divergence and curl operators. The PP and PS imaging conditions are expressed in the frequency domain as follows:

$$I_{PP}(\mathrm{x},\mathrm{z}) = \sum_{s}\sum_{\omega} \nabla \cdot S_s(\omega, x, z) \ \ \nabla \cdot R_s(\omega, x, z), \qquad (3\text{-}3)$$

$$I_{PS}(\mathrm{x},\mathrm{z}) = \sum_{s}\sum_{\omega} \nabla \cdot S_s(\omega, x, z) \ \ \nabla \times R_s(\omega, x, z), \qquad (3\text{-}4)$$

respectively. These images can be normalized by the pseudo Hessian matrix to enhance the amplitude of lower part as follows:

$$I_{PP}(\mathrm{x},\mathrm{z}) = \frac{\sum_s \sum_\omega \nabla \cdot S_s(\omega, x, z) \ \ \nabla \cdot R_s(\omega, x, z)}{\sum_s \sum_\omega \nabla \cdot S_s(\omega, x, z) \ \ \nabla \cdot S_s(\omega, x, z)}, \qquad (3\text{-}5)$$

$$I_{PS}(\mathrm{x},\mathrm{z}) = \frac{\sum_s \sum_\omega \nabla \cdot S_s(\omega, x, z) \ \ \nabla \times R_s(\omega, x, z)}{\sum_s \sum_\omega \nabla \cdot S_s(\omega, x, z) \ \ \nabla \cdot S_s(\omega, x, z)}. \qquad (3\text{-}6)$$

In the case of PS imaging condition, a polarity reversal problem should be considered (Du et al., 2012; Zhang and Shi, 2019). The sign is opposite on the basis of normal line between source and structure because of the curl operator shown in Figure 3-1. When the horizontal layers are dominant, reversal problem can be solved by changing the sign of left side based on source location. Figure 3-2 shows images before and after the polarity reversal correction for the 2-layer model. When one of the receivers was used, the image after the polarity reversal correction becomes symmetric (Figures 3-2a and 3-2b). When all the receivers were used, the image after the polarity reversal correction becomes more accurate (Figures 3-2c and 3-2d).

To investigate the differences between PP and PS imaging conditions, different anomalies are added to the P- and S-wave velocity models of the Volve tomography model (Figure 3-3) obtained by the seismic tomography using Volve oilfield data. Detailed explanations about Volve oilfield data are given in Chapter 4. For synthetic data generated for those models, RTM is applied. The RTM images are displayed in Figure 3-4. Figure 3-4 shows that the PP image is similar to the P-wave velocity model, while the PS image resembles the S-wave velocity model.

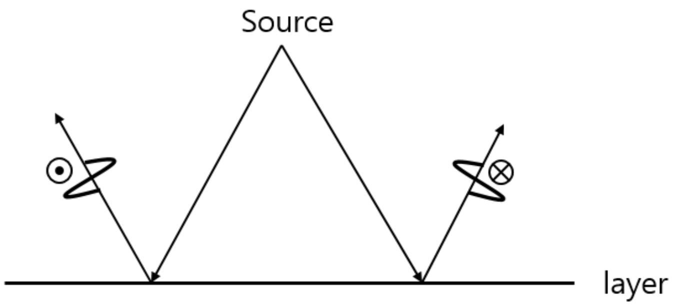

Figure 3-1. The polarity reversal of S-wave separated by the curl operator.

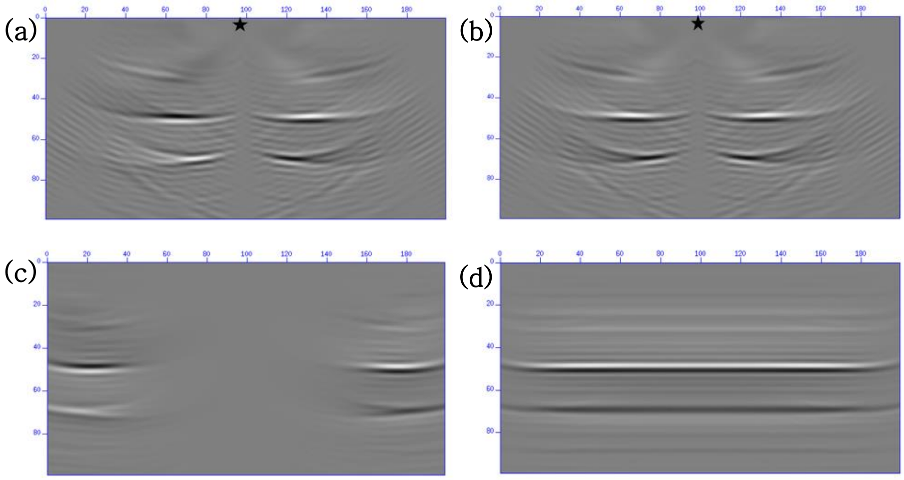

Figure 3-2. RTM images (a, c) before and (b, d) after the polarity reversal correction using (a, b) one source and (c, d) all sources.

(a)

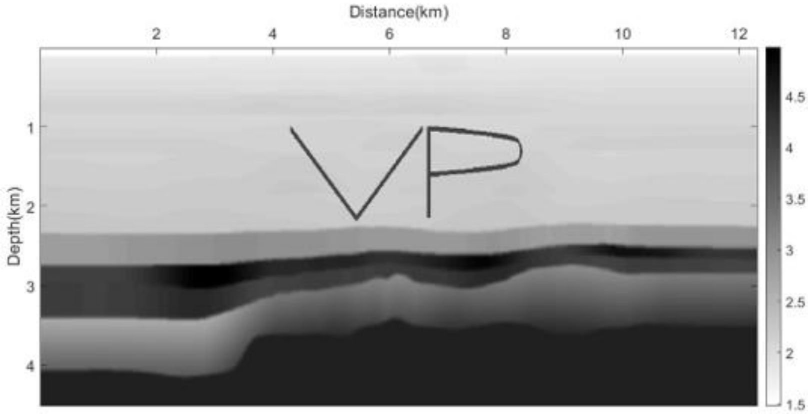

(b)

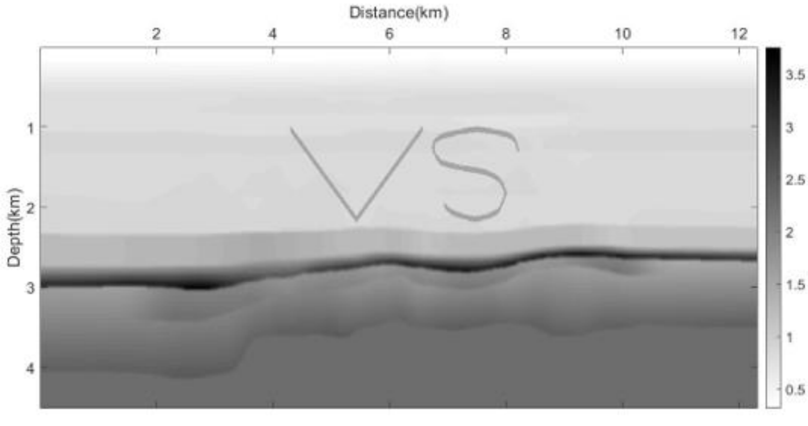

Figure 3-3. Modified Volve tomography models: (a) P- and (b) S-wave velocity models.

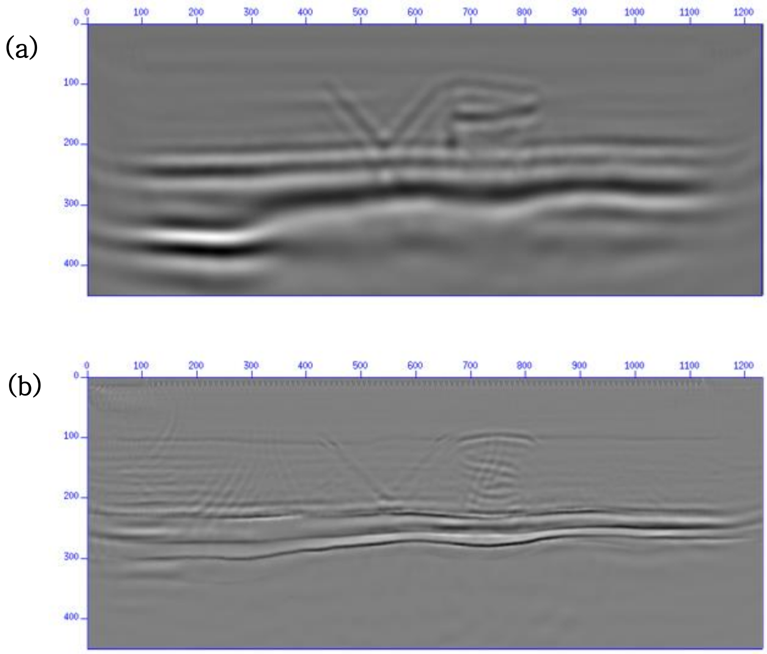

Figure 3-4. RTM images obtained for the modified Volve tomography models: (a) PP and (b) PS imaging conditions.

3.3. Strategy for data component

In case of 2D OBC data, not only pressure data but also horizontal (x-direction) and vertical (z-direction) accelerations are recorded. Therefore, the quality of RTM image can be enhanced by using multicomponent data. To develop a strategy for choosing appropriate data components, PP and PS images are obtained using the x- or z-direction data for the Volve tomography model shown in Figure 3-5. From the images shown in Figure 3-6, it is recommended to use the z-direction data for the PP image and x-direction data for the PS image. The PP image obtained using the x-direction data and the PS image using the z-direction data show vertical artifacts and unclear structures. It may be because signals at far offsets are attenuated and contain noises, while signals at near offsets are strong. At near offsets, vertically propagating waves are dominant. When wave propagates vertically, particles vibrate vertically by the P-wave, and horizontally by the S-wave. Therefore, the z-component data mainly contain the information of P-wave, and the x-component data dominantly include the information of S-wave.

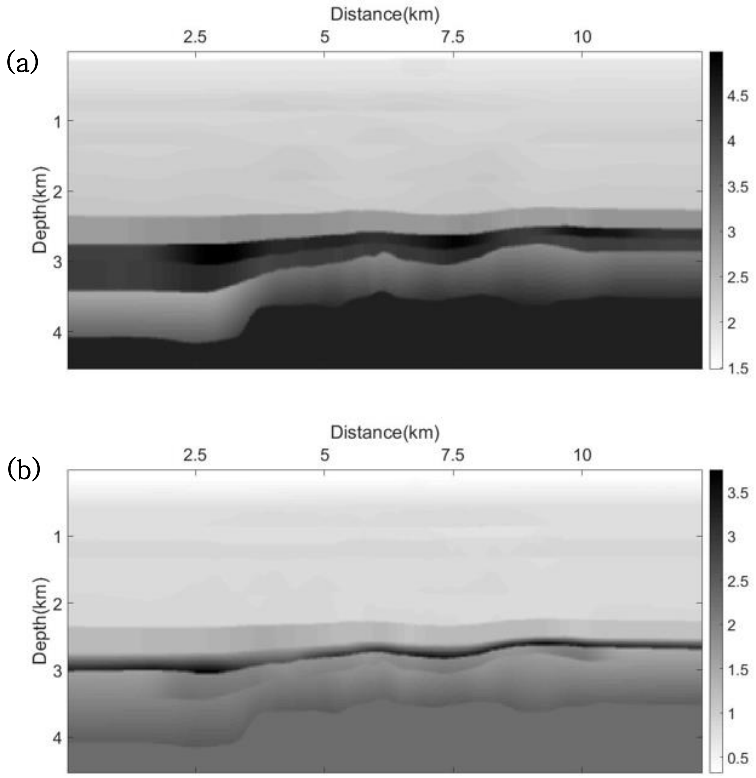

Figure 3-5. Volve tomography model: (a) P- and (b) S-wave velocity models.

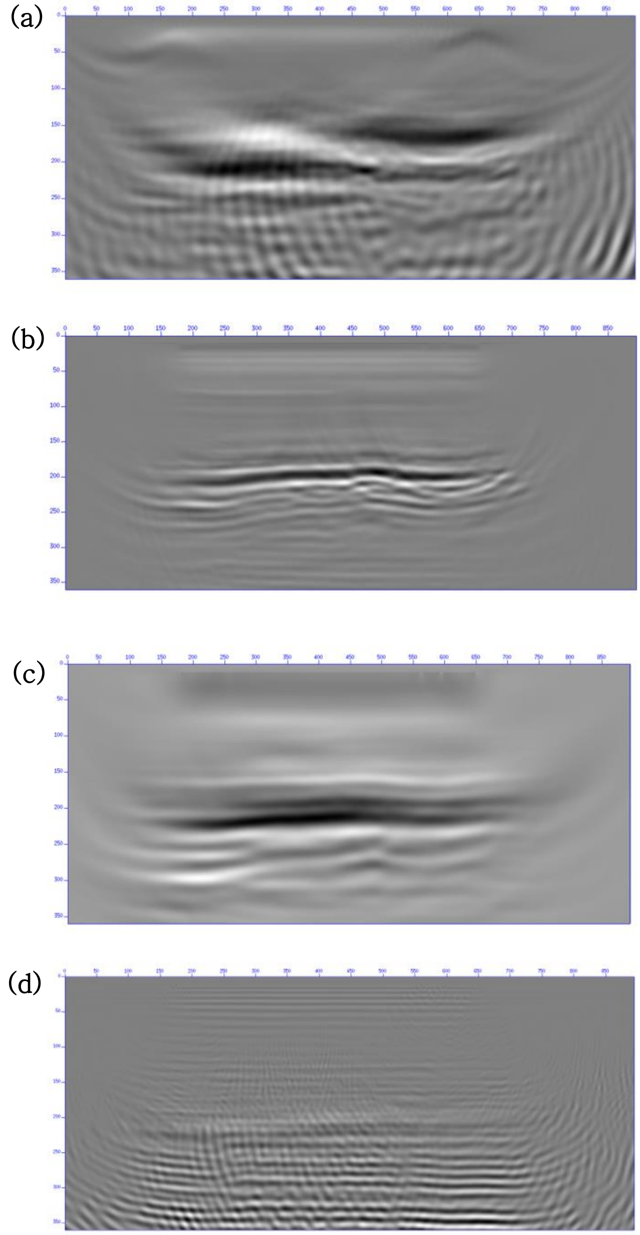

Figure 3-6. RTM images obtained by the (a, b) PP and (c, d) PS imaging conditions using (a, c) horizontal- and (b, d) vertical-component data.

Chapter 4. Real data example: Volve oilfield data in the North Sea

4.1. Data information

The proposed strategy is applied to Volve oilfield data. The Volve data are OBC data recorded in the North Sea in 2010 (Figure 4-1). One cable of 3D data is chosen for 2D elastic RTM (No. 40195-1252860). The shot line and receiver line is on the same plane. 443 shots and 235 receivers were relocated with a grid interval of 12.5 m. The depth of sea bottom is around 100 m, and the geometry of sources and receivers are shown in Figure 4-2. Figure 4-3 shows representative shot gathers. Although the original record length is 10 seconds, only 8 seconds data are used for RTM. A time interval is 2 ms.

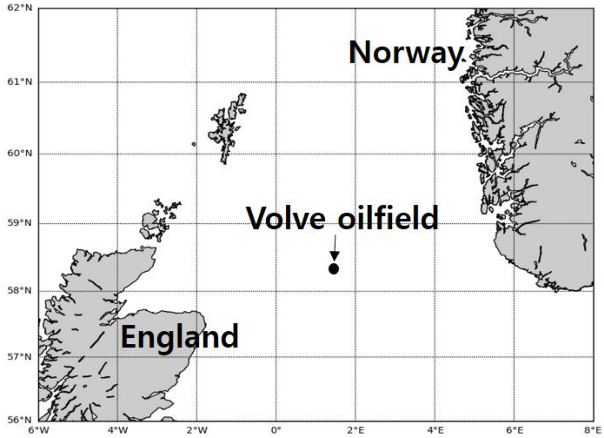

Figure 4-1. The location of the Volve oilfield in the North Sea.

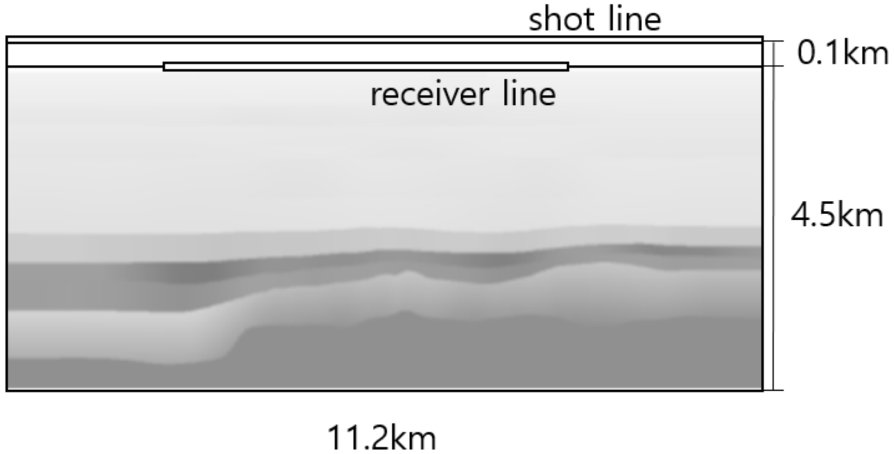

Figure 4-2. The geometry of sources and receiver cables.

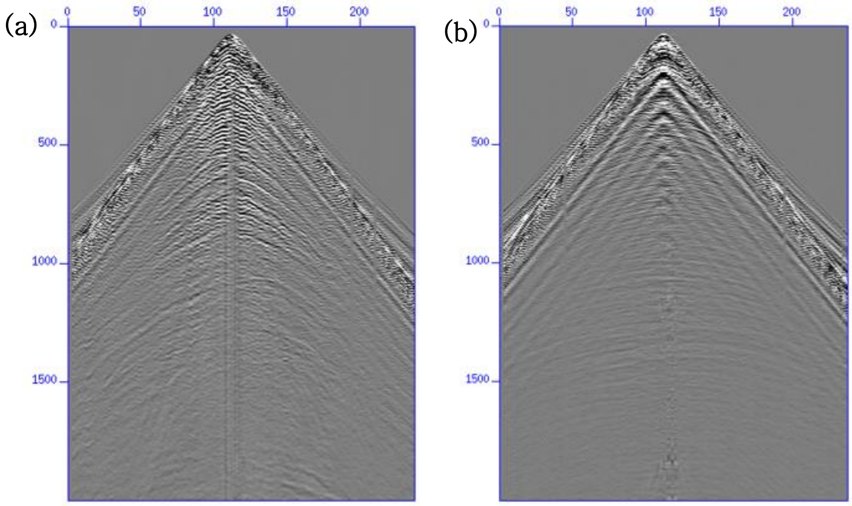

Figure 4-3 A representative shot gather (corresponding to the 200^{th} source) for (a) horizontal and (b) vertical particle accelerations.

4.2. RTM results

If the model used for RTM has discontinuous layers with a large changes of velocity, an amount of energy in waves reaching the boundary is reflected. In this case, unwanted cross-correlation values are calculated, resulting in inaccurate RTM images (Sava and Hill, 2009). Therefore, a smoothed version of the Volve tomography model is used as a background model for RTM (Figure 4-4).

Figure 4-5 shows RTM images obtained using the strategy. This area is known to have a dominant cap rock and horizontal layer. Also, it is known that the upper part of the reservoir is horizontally deposited, and the lower part of the reservoir is interpreted as faults. The RTM images also show the cap rock, layer structures and the irregular structures of the lower part. In Figure 4-5, the differences between P- and S-wave velocity structures are observed.

Figure 4-6 shows the P- and S-wave velocity profiles extracted from the well-log data. Although the ratio of P-wave velocity to S-wave velocity is about 2 in most parts, the ratio reaches 4 around a depth of 2.35 km. In other words, the tendencies of the P- and S-wave velocity structures are similar over the whole model except for the depth of 2.35 km. While the P-wave velocity smoothly varies, the S-wave velocity rapidly decreases. The RTM images also describe these features. The layer at a depth of 2.35 km is described in the PS image, whereas it is not properly depicted in the PP image (Figure 4-5). All of these results demonstrate that the proposed strategy is good for RTM of multicomponent OBC data.

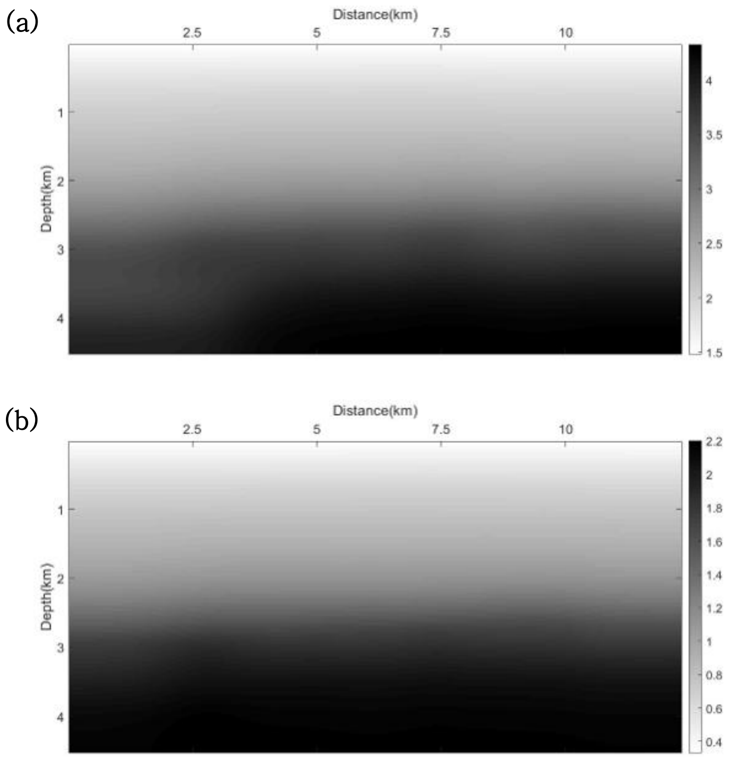

Figure 4-4. A smoothed version of the Volve tomography model: (a) P- and (b) S-wave velocity models.

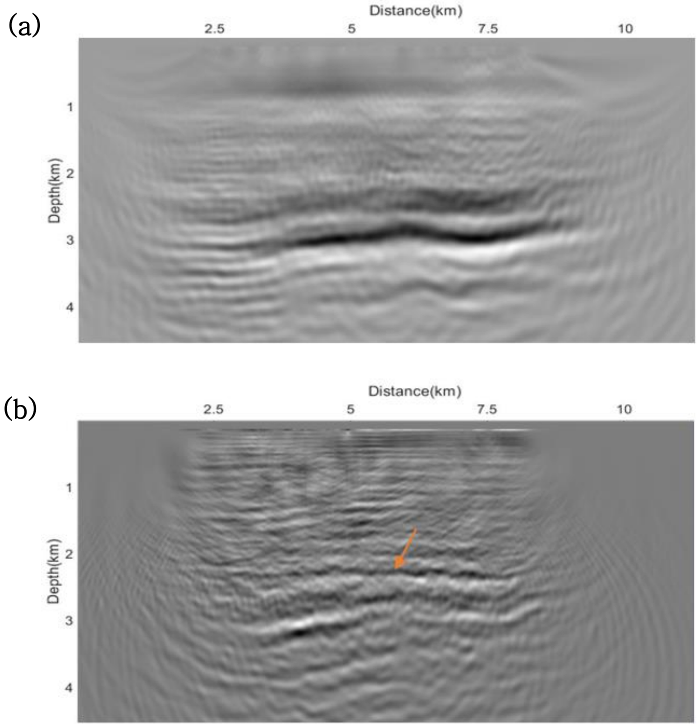

Figure 4-5. RTM images obtained using the (a) PP and (b) PS imaging conditions. The arrow indicates that the layer at a depth of 2.35 km is properly described in the PS image and it is not in the PP image.

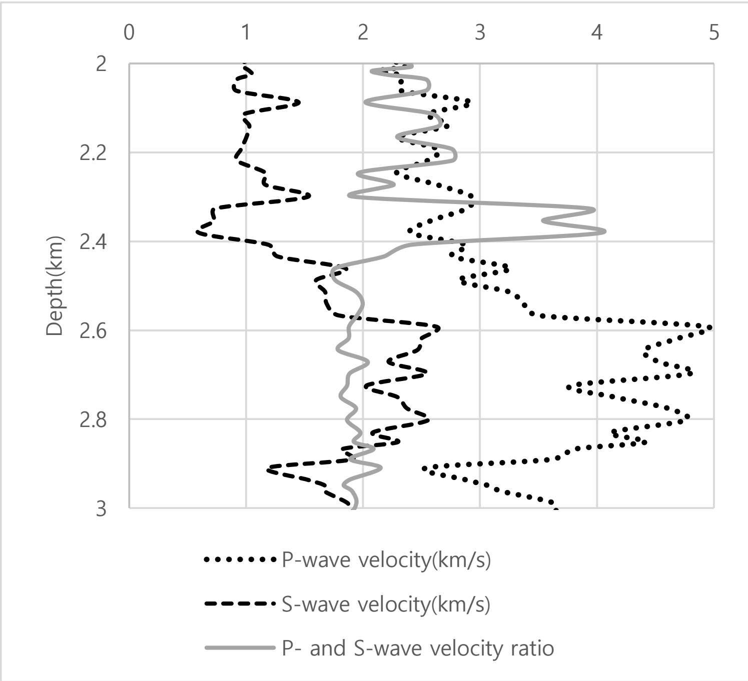

Figure 4-6. Vertical profiles from well log.

Chapter 5. Conclusion

Reverse time migration is one of the effective techniques to image subsurface structures. As multicomponent OBC exploration has been common in recent years, there has been needs for strategies to effectively utilize multicomponent data. In this study, elastic RTM strategy for multicomponent OBC data was studied. Different anomalies were added to the P- and S-wave velocity models and RTM was applied to investigate the differences between PP and PS imaging conditions. In addition, PP and PS images were obtained using the x- or z- direction data to develop the strategy for choosing appropriated data components. Consequently, the strategy was proposed as follows:

1. Using the staggered-grid set for modeling
2. Obtaining the PP image to describe the P-wave structures and the PS image to describe the S-wave structure.
3. Using the z-component data for the PP image and the x-component data for the PS image.

The proposed strategy was applied to the Volve data acquired in the North Sea. Compared to the well-log data, the difference between the P- and S-wave velocity structures is confirmed in the PP and PS images.

Numerical results showed that by using both the PP and PS images, detailed structures can be obtained, and the differences between the PP and PS images can be examined. Because the PS image is not affected by fluid, reservoirs can be monitored by comparing PP image and PS image.

References

Baysal, E., Kosloff, D. D. and Sherwood, J. W. C., 1983. Reverse time migration. *Geophysics*, **48**, 1514-1524.

Berenger, J.-P., 1994. A perfectly matched layer for the absorption of electromagnetic waves. *Journal of computational Physics*, **114**, 185-200.

Chung, W. K., 2011. Frequency domain elastic reverse-time migration using wave-field separation (Doctoral dissertation, Seoul National University).

Collino, F., and Tsogka, C., 1998. Application of the PML absorbing layer model to the linear elastodynamic problem in anisotropic heterogeneous media (Doctoral dissertation, National Institute for Research in Digital Science and Technology).

Du, Q., Zhu, Y., and Ba, J., 2012. Polarity reversal correction for elastic reverse time migration. *Geophysics*, **77(2)**, S31-S41

Graves, R. W., 1996. Simulating seismic wave propagation in 3D elastic media using staggered-grid finite differences. *Bulletin of the Seismological Society of America*, **86(4)**, 1091-1106.

Guitton, A., Kaelin, B., and Biondi, B., 2007. Least-squares attenuation of reverse-time-migration artifacts. *Geophysics*, **72(1)**, R117-R127.

Hwang, J., Oh, J.-W., Lee, J., Min, D.-J., and Jeong, H., 2020. Acoustic Full-waveform inversion strategy for multi-component ocean-bottom cable data. *Geophysics and Geophysical Exploration*, **23(1)**, 38-49.

Jo, C., Shin, C., and Suh, J., 1996. An optimal 9-point, finite-difference, frequency-space, 2-D scalar wave extrapolator. *Geophysics*, **61(2)**, 529-537.

Lailly, P., 1983. The seismic inverse problem as a sequence of before stack migration. In J. B. Bednar, R. Rednar, E. Robinson, and A. Weglein, eds., Conference on inverse scattering: Theory and application. *Society for Industrial and Applied Mathematics*, 206-220.

McMechan, G. A., 1983. Migration by extrapolation of time-dependent boundary values. *Geophysical Prospecting*, **31**, 413-420.

Min, D.-J., Shin, C., and Yoo, H. S., 2004. Free-surface boundary condition in finite-difference elastic wave modeling. *Bulletin of the Seismological Society of America*, **94(1)**, 237-250.

Park, M.-H., Lee, C. S., Kim, B.-Y., Kim, J.-H., Kim, K. J., and Shinn, Y. J., 2018, Preliminary results of the pre-injection monitoring survey at an offshore CO_2 injection site in the Yeongil Bay, *The Journal of Engineering Geology*, **28(2)**, 247-258.

Sava, P., and Hill, S. J., 2009, Overview and classification of wavefield seismic imaging methods, *The Leading Edge*, **28(2)**, 170-183

Schneider, W. A., 1978. Integral formulation for migration in two and three dimensions. *Geophysics*, **43**, 49-76.

Shin, C., Jang, S., and Min, D., 2001. Improved amplitude preservation for prestack depth migration by inverse scattering theory. *Geophysical Prospecting*, **49(5)**, 592-606.

Shin, S. R., Shin, C. S., and Suh, J. H., 1997. Finite difference seismic modeling using staggered grid. *Journal of the Korean Society of Mineral and Energy Resources Engineers*, **34**, 168-174

Shinn, Y. J., Kwon, Y. K., Yoon, J.-R., Kim, B.-Y., and Cheong, S., 2018, Result of CO2 geological storage site survey for small-scale demonstration in Pohang Basin, Yeongil Bay, SE Korea, *The Journal of Engineering Geology*, **28(2)**, 161-174

Tarantola, A., 1984. Inversion of seismic reflection data in the acoustic approximation. *Geophysics*, **49(8)**, 1259-1266.

Virieux, J., 1984. SH-wave propagation in heterogeneous media: Velocity-stress finite-difference method. *Geophysics*, **49(11)**, 1933-1957.

Whitemore, N. D., 1983. Iterative depth migration by backward time propagation. *53rd SEG meeting, Expanded Abstract*, 827-830.

Yan, J., and Sava, P., 2008. Isotropic angle-domain elastic reverse-time migration. *Geophysics*, **73(6)**, S229-S239.

Zhang, W., and Shi, Y., 2019. Imaging condition for elastic reverse time migration. *Geophysics*, **84(2)**, S95-S111.

초 록

다성분 해저면 탄성파 탐사자료 역시간 구조보정 전략

이 진 형
에너지시스템공학부
서울대학교 대학원

역시간 구조보정은 복잡한 지형에서도 지하구조를 정확히 영상화하는 자료처리 방법이다. 최근 하이드로폰과 지오폰이 결합된 수진기를 해저면에 설치하여 탐사하는 다성분 해저면 탄성파 탐사가 증가하는 추세이다. 다성분 해저면 탄성파 탐사는 신호를 더 가까이서 기록하고, 커버리지가 넓으며, 더 많은 정보를 얻을 수 있다는 장점이 있다. 이에 따라 다성분 해저면 탄성파 자료를 활용하기 위한 연구가 필요해졌다.

이 연구에서는 다성분 해저면 탄성파 자료를 이용한 역시간 구조보정 전략을 제시하였다. 모델링 격자는 해저면 환경에서 장점이 있는 엇격자를 이용하였으며, 영상화 조건과 자료 성분에 따라 구조보정 영상에 미치는 영향을 합성 탄성파 자료를 통해 확인하였다. 그 결과, P파 속도구조 구축을 위해서는 z성분 자료를 이용하여 PP 이미지를 영상화하고, S파 속도구조 구축을 위해서는 x성분 자료를 이용하여 PS 이미지를 영상화하는 것이 효과적임을 제안하였다.

제안한 전략을 북해 Volve oilfield 현장 자료에 적용하여 타당성을 확인하였다. 역시간 구조보정 영상이 알려진 지질구조들을 영상화한 것을 확인할 수 있었다. 특히, 검층 자료를 통해 P파와 S파의 속도구조가 상이하게 변화하는 깊이를 확인하였고, 역시간 구조보정을 통해 얻은 PP영상과 PS영상에서도 이러한 차이를 확인할 수 있었다.

주요어: 역시간 구조보정, 탄성 매질, 해저면 탐사, 엇격자, PS 분리
학번: 2019-28629